PCCP

ARTICLE TYPE

Cite this: DOI: 00.0000/xxxxxxxxxx

Reduced-dimensional surface hopping with offline–online computations†

Zachary Morrow,[a] Hyuk-Yong Kwon,[b] C. T. Kelley,*[a] and Elena Jakubikova*[b]

Received Date
Accepted Date

DOI: 00.0000/xxxxxxxxxx

Molecular dynamics simulations often classically evolve the nuclear geometry on adiabatic potential energy surfaces (PESs), punctuated by random hops between energy levels in regions of strong coupling, in an algorithm known as *surface hopping*. However, the computational expense of integrating the geometry on a full-dimensional PES and computing the required couplings can quickly become prohibitive as the number of atoms increases. In this work, we describe a method for surface hopping that uses only important reaction coordinates, performs all expensive evaluations of the true PESs and couplings only once before simulating dynamics (offline), and then queries the stored values during the surface hopping simulation (online). Our Python codes are freely available on GitHub. Using photodissociation of azomethane as a test case, this method is able to reproduce experimental results that have thus far eluded *ab initio* surface hopping studies.

1 Introduction

Many important phenomena in chemistry are the result of nonadiabatic, femtosecond-level quantum transitions between electronic states.[1] Light-induced electronic transitions, for example, have attracted considerable recent study.[2] Applications include the mechanism of vision,[3,4] photophysics of DNA,[5] photocatalysis,[6–8] photovoltaics,[9–13] and spectroscopy.[14–16] Due to the computational expense of simulating nonadiabatic processes with a fully quantum mechanical treatment, modern techniques favor a mixed quantum–classical dynamics (MQCD) approach.[1,17] A popular and straightforward MQCD framework is the Ehrenfest (mean-field) method, where the nuclei evolve classically on a single potential energy surface (PES) that is the weighted average of the different quantum states.[18,19] However, the mean-field approach is generally only valid in regions with weak coupling or similar nuclear behavior between quantum states.[1]

Trajectory-based approaches seek to overcome the limitations of the pure mean-field approximation by using multiple PESs and computing PES couplings along a classical trajectory.[2] Indeed, these methods have become immensely popular over the last two and a half decades.[1,2] Two of the most popular trajectory-based methods are multiple spawning[20–23] and surface hopping.[24–28] Multiple spawning begins with Gaussian wave packets centered around the classical trajectory on a given PES and stochastically spawns new wave packets on a different PES when the classical trajectory approaches a conical intersection.[22] In this way, dynamics proceed on multiple PESs simultaneously. In surface hopping, however, the trajectory marches along a given PES and intermittently hops between surfaces in regions of strong coupling. Each surface hopping simulation runs on exactly one PES at any given time. The framework of multiple spawning treats quantum effects more rigorously from first principles,[2] while surface hopping is attractive because it is straightforward to implement and analyze. The two methods typically produce similar results at similar costs if time integration is done efficiently.[2] Due to its ubiquity and simplicity, surface hopping is the MQCD approach we utilize in this work.

Computing the nonadiabatic coupling (NAC) vector required for surface hopping is an area of much recent activity, enabled by advances in computing power.[29–31] However, the computational expense of time-dependent density functional theory (TD-DFT) is still large enough that it is impractical to query the *ab initio* excitation energies and nonadiabatic couplings at each time point of every trajectory in the surface-hopping swarm.

Furthermore, the full $(3N-6)$-dimensional PES $\mathscr{E}_i(\boldsymbol{x})$ of an N-atom molecule in electronic state i typically includes only a handful of relevant reaction coordinates for a particular reaction. One can partition the geometry into the relevant coordinates (called *design variables*, $\boldsymbol{q} \in \mathbb{R}^d$) and everything else (called *remainder variables*, $\boldsymbol{\xi} \in \mathbb{R}^{3N-6-d}$). Then the so-called "relaxed PES" comes from optimizing over the remainder variables to produce a sur-

[a] Department of Mathematics, Box 8205, North Carolina State University, Raleigh, NC 27695-8205, USA. E-mail: tim_kelley@ncsu.edu
[b] Department of Chemistry, Box 8204, North Carolina State University, Raleigh, NC, 27695-8204, USA. E-mail: ejakubi@ncsu.edu

† Electronic Supplementary Information (ESI) available: Details of sparse interpolation and electronic structure calculations (pdf), PES and nonadiabatic coupling data (xlsx), selected animations of geometry and trajectory (mp4). See DOI: 00.0000/00000000.

face that is only a function of the design variables:

$$E_i(\boldsymbol{q}) = \min_{\boldsymbol{\xi}} \mathscr{E}_i(\boldsymbol{q}, \boldsymbol{\xi}) . \tag{1}$$

We use the relaxed PES in this paper to reduce the dimension of the problem, but the optimization over $\boldsymbol{\xi}$ is still computationally costly.§ The selection of design variables is an important and challenging aspect of chemical dynamics,[32] which our method does not directly address. Frequently, important coordinates are chosen based on trial-and-error or chemical intuition, though automated selection based on principal component analysis (PCA) of a full-dimensional molecular dynamics (MD) simulation has been proposed.[33] Due to the presence of existing work on our model molecule and expense of running a $(3N-6)$-dimensional dynamics trajectory, we use the design variables from previous studies, which we will describe later in greater detail.

Since evaluating the full or relaxed PES with an electronic structure program is computationally expensive, construction of surrogate PESs is an active area of research. These surrogates allow the costly optimizations to be contained as an up-front cost in the offline phase, incurred only when first constructing the surrogate. Techniques of surrogate PES construction include permutationally invariant polynomials,[34–37] neural networks,[38–40] interpolative moving least-squares,[41–44] modified Shepard interpolation,[45–48] Gaussian processes,[49,50] and the finite-element method.[51] Previous work in our group has approximated PESs with sparse interpolation. To build the surrogate, one simply needs to evaluate the true PES in the offline phase at a set of known design variable values $\{\boldsymbol{q}^j\}$. The Smolyak sparse interpolation algorithm ensures that the number of nodes $\boldsymbol{q}^j$ grows polynomially—rather than exponentially—in d, the number of design variables.[52–55] In addition, a relaxed reduced-dimensional molecular dynamics (rr-MD) method, also from our group, allows for online MD simulations of the design variables only.[56]

Construction of surrogate PESs with sparse interpolation in our group has used polynomial,[9,57,58] trigonometric,[59,60] and mixed polynomial–trigonometric[61] basis functions. The original development of trigonometric surrogate PESs occurred because energy would not be conserved in NVE¶ rr-MD simulations with a polynomial surrogate PES if a component of $\boldsymbol{q}$ were periodic and crossed the periodic boundary.[60,61] Implementations of the rr-MD method exist in both polynomial[56] and mixed[61] basis settings.

This paper presents an implementation of Tully's fewest-switches surface hopping (FSSH) algorithm[25] in a reduced-dimensional framework (rr-FSSH) where all expensive electronic structure calculations are performed in the offline phase. This method focuses only on a reduced-dimensional version of "standard" FSSH, though various corrections to FSSH have been proposed in order to account for different phenomena[1] and could be a fruitful area of future work in a reduced-dimensional setting. We organize the remainder of this paper as follows. In Section 2, we describe the computational details of our method: reduced-dimensional molecular dynamics, reduced-dimensional surface hopping, sparse grids, and the approximation of nonadiabatic couplings. In Section 3, we test our method on the photodissociation of azomethane in vacuo and compare against known experimental[62–65] and *ab initio*[66–73] results. Conclusions are in Section 4.

§ Hereafter, if we say "PES" without qualification, we refer to the relaxed PES.

¶ Microcanonical ensemble; conserves number of particles in the system (N), volume (V), and energy (E).

2 Computational Methods

In this section, we describe our online and offline computational methods. In the online phase, we run a swarm of molecular dynamics trajectories that rely on the surrogate PESs and NACs. In the offline phase, we use electronic structure programs to evaluate the required high-fidelity ground-state energies, excitation energies, and coupling vectors. While all methods in this section appear in the online phase, the first two subsections comprise the bulk of the online simulation, and the latter two subsections illuminate the quantities to compute offline.

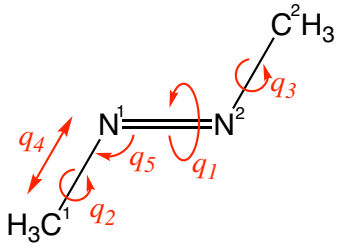

Fig. 1 Azomethane with design variables labeled.

2.1 Reduced-dimensional MD

We briefly summarize the NVE ensemble within the rr-MD framework originally developed by Liu and coworkers.[56] The design variables $\boldsymbol{q}$ and generalized momenta $\boldsymbol{p}$ evolve classically according to Hamiltonian dynamics:[74,75]

$$\begin{cases} \dot{\boldsymbol{q}} &= \nabla_{\boldsymbol{p}} H \\ \dot{\boldsymbol{p}} &= -\nabla_{\boldsymbol{q}} H \end{cases} \tag{2}$$

with the initial conditions $\boldsymbol{q}(0) = \boldsymbol{q}_0$ and $\boldsymbol{p}(0) = \boldsymbol{p}_0$. Here, $H = H(\boldsymbol{q}, \boldsymbol{p})$ is the classical Hamiltonian, expressed as a sum of potential and kinetic energy:

$$H(\boldsymbol{q}, \boldsymbol{p}) = V(\boldsymbol{q}) + K(\boldsymbol{q}, \boldsymbol{p}) . \tag{3}$$

In our context, $V(\boldsymbol{q})$ is the relaxed PES and $K(\boldsymbol{q}, \boldsymbol{p})$ involves the curvilinear mass-metric tensor $\boldsymbol{G}$:

$$K(\boldsymbol{q}, \boldsymbol{p}) = \frac{1}{2} \boldsymbol{p}^T \boldsymbol{G}^{-1}(\boldsymbol{q}) \boldsymbol{p}, \tag{4}$$

$$G_{ij}(\boldsymbol{q}) = \sum_{k=1}^{3N} m_k \frac{\partial X_k(\boldsymbol{q})}{\partial q_i} \frac{\partial X_k(\boldsymbol{q})}{\partial q_j} . \tag{5}$$

The function $\boldsymbol{X} : \mathbb{R}^d \to \mathbb{R}^{3N}$ is a mapping from the design variables to the optimized Cartesian molecular geometry, and m_k is the atomic mass of atom $\texttt{ceil}(k/3)$. $\boldsymbol{X}(\boldsymbol{q})$ is formatted so that the first three components are the (x, y, z) coordinates of atom 1 and

so on. From Equations (3)-(5), we see that we must construct surrogates of $V(\boldsymbol{q})$ and $\boldsymbol{X}(\boldsymbol{q})$ for use in the online phase.

If we have previous dynamics history, we take $\boldsymbol{q}_0$ and $\boldsymbol{p}_0$ to be the geometry and momenta at the last time step. If not, we select a desired starting geometry $\boldsymbol{q}_0$ and construct $\boldsymbol{p}_0$ as follows. We first choose a starting temperature T and draw $3N$ Cartesian velocities $\boldsymbol{v}_0$ from a Boltzmann distribution:

$$\boldsymbol{v}_0 = \sqrt{k_B \boldsymbol{M}^{-1} T}\, \boldsymbol{R}_t\,, \tag{6}$$

where $\boldsymbol{R}_t$ is a $3N$-dimensional standard normal random variable[||] realized at time t, k_B is the Boltzmann constant in appropriate units, and $\boldsymbol{M} = \mathrm{diag}(m_1,\ldots,m_{3N})$. We then project $\boldsymbol{v}_0$ onto the design variable space by setting

$$\boldsymbol{p}_0 = \boldsymbol{X}'(\boldsymbol{q}_0)^T\, \boldsymbol{v}_0, \qquad (\boldsymbol{X}'(\boldsymbol{q}))_{ij} = \frac{\partial X_i(\boldsymbol{q})}{\partial q_j}\,. \tag{7}$$

We integrate the system forward in time using the Störmer–Verlet method.[76,77]

2.2 Reduced-dimensional FSSH

We now present the reduced-dimensional adaptation of Tully's immensely popular fewest-switches surface hopping (FSSH) method.[25] As noted previously, various modifications of FSSH have been proposed in order to account for different phenomena,[1] such as nuclear quantum effects,[78] decoherence,[79] quantum interference,[25] and representation-dependence.[80] However, the aim of this paper is to use "standard" FSSH[25,26] as a starting point for a reduced-dimensional surface hopping paradigm where the various corrections of FSSH can also be implemented in the future.

We let $\hat{H}_0(\boldsymbol{z};\boldsymbol{X})$ denote the electronic Hamiltonian, where $\boldsymbol{z}$ is the electronic coordinate and $\boldsymbol{X} \in \mathbb{R}^{3N}$ is the Cartesian geometry of the molecule. We opt to use the orthonormal eigenfunctions $\Phi_j(\boldsymbol{z};\boldsymbol{X})$ of $\hat{H}_0$ as the expansion basis. With this choice, we define the matrix elements

$$V_{ij}^{cart}(\boldsymbol{x}) = \langle \Phi_i(\boldsymbol{z};\boldsymbol{X}) | \hat{H}_0(\boldsymbol{z};\boldsymbol{X}) | \Phi_j(\boldsymbol{z};\boldsymbol{X}) \rangle = \mathscr{E}_i(\boldsymbol{X})\delta_{ij} \tag{8}$$

where $\mathscr{E}_i(\boldsymbol{X})$ is the full PES of state i as a function of Cartesian geometry, δ_{ij} is the Kronecker delta, and the brackets denote integration over $\boldsymbol{z}$. In Tully's original formulation, the nonadiabatic coupling vector in Cartesian coordinates is

$$\boldsymbol{d}_{ij}^{cart}(\boldsymbol{X}) = \langle \Phi_i(\boldsymbol{z};\boldsymbol{X}) | \nabla_{\boldsymbol{X}} \Phi_j(\boldsymbol{z};\boldsymbol{X}) \rangle\,. \tag{9}$$

However, we now want the couplings in terms of the design variables $\boldsymbol{q}$. Since $\boldsymbol{X} = \boldsymbol{X}(\boldsymbol{q})$ reconstructs the Cartesian geometry after optimizing the remainder variables, we get

$$V_{ij}(\boldsymbol{q}) = E_i(\boldsymbol{q})\delta_{ij} \tag{10}$$

[||] That is, $\boldsymbol{R}_t \in \mathbb{R}^{3N}$ where each component is independent and normally distributed with mean $\mu = 0$ and standard deviation $\sigma = 1$.

The chain rule yields

$$\boldsymbol{d}_{ij}(\boldsymbol{q}) = \langle \Phi_i(\boldsymbol{z};\boldsymbol{X}(\boldsymbol{q})) | \nabla_{\boldsymbol{q}} \Phi_j(\boldsymbol{z};\boldsymbol{X}(\boldsymbol{q})) \rangle = \boldsymbol{X}'(\boldsymbol{q})^T\, \boldsymbol{d}_{ij}^{cart}(\boldsymbol{X}(\boldsymbol{q}))\,. \tag{11}$$

We now express the wavefunction of the electronic state of our system at time t in terms of the electronic basis functions

$$\Psi(\boldsymbol{z},\boldsymbol{q},t) = \sum_j c_j(t)\Phi_j(\boldsymbol{z};\boldsymbol{q}) \tag{12}$$

where we have expressed dependence directly in terms of $\boldsymbol{q}$ for notational ease. Combining (12) with the time-dependent Schrödinger equation, we may derive

$$\mathrm{i}\hbar \dot{c}_k = \sum_j \left(E_k(\boldsymbol{q})\delta_{kj} - \mathrm{i}\hbar \dot{\boldsymbol{q}} \cdot \boldsymbol{d}_{kj}(\boldsymbol{q}) \right) c_j\,. \tag{13}$$

With adiabatic electronic wavefunctions, the probability of transition from state i to state j during a time interval $[t, t+\Delta t]$ is[25,26]

$$P(i \to j) = \max\left\{ 2\,\mathrm{Re}\left(\frac{c_j}{c_i}\, \dot{\boldsymbol{q}} \cdot \boldsymbol{d}_{ij}(\boldsymbol{q}) \right) \Delta t,\ 0 \right\}. \tag{14}$$

We integrate (13) with the Crank–Nicolson method,[81,82] which conserves the ℓ^2 norm of the solution, so that all state occupations sum to 1. The time step required to integrate (13) accurately is much smaller than that used for the classical dynamics (2), so we linearly interpolate all relevant quantities during intermediate steps.[25,26]

The transition probability in (14) is evaluated at each classical time step. If a switch from state i to j occurs at $t = t_n$ and $E_j(\boldsymbol{q}_n) \neq E_i(\boldsymbol{q}_n)$, then we must adjust the momentum $\boldsymbol{p}_n$ to conserve total energy.[25] Similarly to Hammes–Schiffer and Tully,[26] we set

$$\boldsymbol{p}_n^{corr} = \boldsymbol{p}_n - \alpha\, \boldsymbol{d}_{ij}(\boldsymbol{q}_n) \tag{15}$$

and solve for α in light of (3)-(5), yielding the equation

$$\frac{1}{2}(\boldsymbol{d}^T \boldsymbol{G}^{-1} \boldsymbol{d})\alpha^2 - (\boldsymbol{p}^T \boldsymbol{G}^{-1} \boldsymbol{d})\alpha + (E_j - E_i) = 0\,. \tag{16}$$

Above, for notational simplicity, $\boldsymbol{d} = \boldsymbol{d}_{ij}$ and all quantities are evaluated at $t = t_n$ or $\boldsymbol{q} = \boldsymbol{q}_n$. If $E_j > E_i$ and momentum is insufficient to overcome the energy gap, i.e.

$$(\boldsymbol{p}^T \boldsymbol{G}^{-1} \boldsymbol{d})^2 - 2(\boldsymbol{d}^T \boldsymbol{G}^{-1} \boldsymbol{d})(E_j - E_i) < 0, \tag{17}$$

then we have a frustrated hop. In this case, we reflect momentum in the direction of $\boldsymbol{d}$ by setting

$$\alpha = 2\,\frac{\boldsymbol{p}^T \boldsymbol{G}^{-1} \boldsymbol{d}}{\boldsymbol{d}^T \boldsymbol{G}^{-1} \boldsymbol{d}}\,. \tag{18}$$

If, however, the inequality in (17) is reversed and two solutions of (16) exist, we have

$$\alpha = \frac{(\boldsymbol{p}^T \boldsymbol{G}^{-1} \boldsymbol{d}) \pm \sqrt{(\boldsymbol{p}^T \boldsymbol{G}^{-1} \boldsymbol{d})^2 - 2(\boldsymbol{d}^T \boldsymbol{G}^{-1} \boldsymbol{d})(E_j - E_i)}}{\boldsymbol{d}^T \boldsymbol{G}^{-1} \boldsymbol{d}} \tag{19}$$

and we take the "+" solution if $\boldsymbol{p}^T \boldsymbol{G}^{-1} \boldsymbol{d} < 0$ and the "−" solution otherwise.[26] We then proceed with the dynamics in (2) using $V(\boldsymbol{q}) = E_j(\boldsymbol{q})$, $\boldsymbol{q} = \boldsymbol{q}_n$, and $\boldsymbol{p} = \boldsymbol{p}_n^{corr}$.

2.3 Sparse interpolation

We use mixed-basis interpolation for the surrogate PESs since azomethane photodissociation involves both periodic and nonperiodic coordinates (see Fig. 1).[61,68] The notation of sparse grids can be rather dense, so we suppress some of the mathematical details here for the sake of brevity and clarity. The interested reader can find a much fuller account in the ESI, Sec. 1.†

Generally, the single-basis interpolant of a target function $f : [0,1]^d \to \mathbb{R}$ is given by[53,59,82]

$$G[f](\boldsymbol{q}) = \sum_{j=1}^{M} c_j \phi_j(\boldsymbol{q}) \tag{20}$$

where ϕ_j are interpolation basis functions and c_j are interpolation coefficients. Though the canonical domain of each component is $[0,1]$, the domain can be shifted to any closed interval using a simple affine transformation. Computing c_j requires the values $f(\boldsymbol{q}_j)$ at a set of nodes $\{\boldsymbol{q}_j\}_{j=1}^{M}$ such that

$$G[f](\boldsymbol{q}_j) = f(\boldsymbol{q}_j), \qquad j = 1,\ldots,M. \tag{21}$$

If $d > 1$, then ϕ_j are products of one-dimensional basis functions $\ell_i(x)$:

$$\phi_j(\boldsymbol{q}) = \prod_{k=1}^{d} \ell_{i_k(j)}(q_k) \tag{22}$$

where $i_k(j)$ is the interpolation level in dimension k corresponding to node j. The advantage of sparse grids is to choose $i_k(j)$ so that the ϕ_j in (20) are the dominant modes in the L^2 expansion of f, e.g. in a Fourier[59] or Legendre[53] series. In this way, we require fewer nodes to obtain a given level of approximation accuracy, improving the overall numerical convergence rate compared to interpolation with tensor-product grids.[53,54,59]

Now we turn our attention to the mixed-basis construction.[61] The Lagrange polynomials with Clenshaw–Curtis[83] points $\{x_j\}$ are a popular choice of $\ell_j(x)$ for nonperiodic f:

$$\ell_j(x) = \prod_{i=0,\ i\neq j}^{m} \frac{x - x_i}{x_j - x_i}. \tag{23}$$

The corresponding interpolation coefficients in one dimension are $c_j = f(x_j)$. For periodic f, a trigonometric basis $\ell_j(x)$ that will preserve the periodicity of the gradient is[55,59]

$$\ell_j(x) = \exp\left(2\pi \mathrm{i} \cdot \sigma(j) \cdot x\right), \qquad j = 0,\ldots,m$$

$$\sigma(j) = \begin{cases} -j/2, & j \text{ even} \\ (j+1)/2, & j \text{ odd} \end{cases}.$$

Here, the one-dimensional interpolation coefficients c_j come out of a discrete Fourier transform of $f(x_j)$ at equally spaced nodes. The polynomial and trigonometric interpolation rules that we use are nested with respect to the level. As a result, we only need to evaluate the *additional* points when we refine the grid.

Since the two basis choices have interpolation coefficients with different forms, we need to rewrite (20) differently in order to combine polynomial and trigonometric interpolation. We may rewrite the single-basis sparse interpolant (20) in adjoint form[84] as

$$G[f](\boldsymbol{q}) = \sum_{j=1}^{M} f(\boldsymbol{q}_j)\psi_j(\boldsymbol{q}) \tag{24}$$

for some adjoint functions ψ_j. With (24), we can create one sparse grid for periodic components and one for nonperiodic components, take their tensor product, and combine them as follows:

$$G_{mix}[f](\boldsymbol{q}) = \sum_{i=1}^{M_{trig}} \sum_{j=1}^{M_{poly}} f(\boldsymbol{\alpha}_i, \boldsymbol{\beta}_j)\, \psi_i^{trig}(\boldsymbol{\alpha})\, \psi_j^{poly}(\boldsymbol{\beta}). \tag{25}$$

In (25), we have partitioned $\boldsymbol{q}$ into the periodic components $\boldsymbol{\alpha}$ and the nonperiodic components $\boldsymbol{\beta}$. Because the two sparse grids are independent, the number of nodes, number of components, and decay patterns of the dominant L^2 coefficients can be controlled separately. We use the Tasmanian package to handle all sparse interpolation.[53,59,84–86] In the context of PES approximation, we must compute the values of $E_n(\boldsymbol{q})$ and $\boldsymbol{X}(\boldsymbol{q})$ at the nodes $(\boldsymbol{\alpha}_i, \boldsymbol{\beta}_j)$ in the offline phase.

2.4 Approximation of nonadiabatic couplings

The computation of $\boldsymbol{d}_{ij}^{cart}$ in (9) is relatively costly, so we would like to avoid doing it at every time step in the online phase. The Landau–Zener formula[87–89] is a popular approach to computing the transition probability (14) because it avoids NACs and is derived from first principles. However, the Landau–Zener formula is only applicable where the energy difference $E_i(\boldsymbol{q}) - E_j(\boldsymbol{q})$ is at a local minimum along the trajectory $\boldsymbol{q} = \boldsymbol{q}(t)$.[90,91] Another possibility is to define custom diabatic wavefunctions that allow for easier evaluation of the NACs,[67] but such methods tend to be molecule-specific. We desire a general, molecule-impartial method of querying the transition probability at all time steps and not only those corresponding to a local minimum of the energy difference along the trajectory.

Many components of the coupling vector will peak sharply in a small region and be zero over large portions of the design variable domain, behavior which is not amenable to interpolation with globally defined basis functions. As a result, we compute $\boldsymbol{d}_{ij}^{cart}$ in the offline phase at a list of design variable values known mathematically to possess a space-filling property known as *low discrepancy*.[92,93] At every time point in the online phase, we approximate the NAC along the simulation trajectory using the known coupling at the nearby space-filling points.

We obtain the space-filling points from the Sobol' sequence,[94] which is implemented in MATLAB and part of a class of sequences known as quasi-random. Such sequences are deterministic but fill a domain in much the same way that uniformly distributed random variables would. However, the number of quasi-random points needed to fill a domain is much lower than that of random variables. Quasi-random sequences are the core of quasi-Monte Carlo integration, which has significantly faster convergence than fully stochastic Monte Carlo techniques[92,93] and is an active area of research.[95–98]

Using MATLAB, we obtain a set of Sobol' points $\{\boldsymbol{q}_m^{sobol}\} \subset [0,1]^d$ such that no point is more than 0.02 away from its nearest neighbor. We then transform these points, in place, by converting each

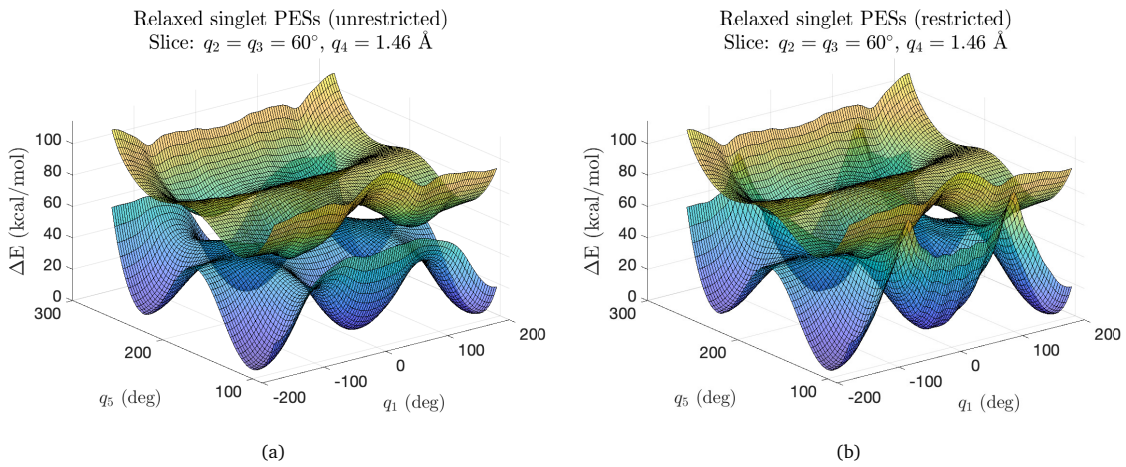

(a) (b)

Fig. 2 (a) Mixed-basis S_0 and S_1 PESs (kcal/mol) with stability-checked wavefunctions. Energies are relative to the optimized *trans*- structure. (b) PESs using restricted wavefunctions.

component of $\boldsymbol{q}_m^{sobol}$ from $[0,1]$ to the corresponding physical domain (see Table 1). We evaluate the Cartesian NACs (9) at the geometries $\boldsymbol{X}(\boldsymbol{q}_m^{sobol})$, $m = 1,\ldots,N_{sobol}$.

At time $t = t_n$ in the online phase, we approximate $\boldsymbol{d}_{ij}^{cart}(\boldsymbol{q}_n)$ as the weighted average of all $\boldsymbol{d}_{ij}^{cart}(\boldsymbol{q}_m^{sobol})$ within some user-adjustable radius R of $\boldsymbol{q}_n$. (For notational simplicity, we express dependence of $\boldsymbol{d}_{ij}^{cart}$ only on $\boldsymbol{q}$.) We define the set

$$S_n(R) = \{m \in \mathbb{N}, : \|\boldsymbol{D}^{-1}(\boldsymbol{q}_m^{sobol} - \boldsymbol{q}_n)\|_2 \leq R\}, \tag{26}$$

where $\boldsymbol{D}$ is a diagonal matrix with D_{ii} being the length of the physical domain of component q_i. We include $\boldsymbol{D}$ to account for different length scales across components. If $S_n(R)$ is empty, then we use the nearest neighbor:

$$\boldsymbol{d}_{ij}^{cart}(\boldsymbol{q}_n) \approx \boldsymbol{d}_{ij}^{cart}\left(\underset{1\leq m\leq N_{sobol}}{\arg\min} \|\boldsymbol{D}^{-1}(\boldsymbol{q}_m^{sobol} - \boldsymbol{q}_n)\|_2\right). \tag{27}$$

Otherwise, we compute the weights

$$w_m = \frac{b_m}{\sum_{k\in S_n(R)} b_k}, \qquad m \in S_n(R),$$

$$b_m = \exp\left(-\frac{\|\boldsymbol{D}^{-1}(\boldsymbol{q}_m^{sobol} - \boldsymbol{q}_n)\|_2}{\min_{k\in S_n(R)} \|\boldsymbol{D}^{-1}(\boldsymbol{q}_k^{sobol} - \boldsymbol{q}_n)\|_2}\right), \qquad m \in S_n(R),$$

and take

$$\boldsymbol{d}_{ij}^{cart}(\boldsymbol{q}_n) \approx \sum_{m\in S_n(R)} w_m \boldsymbol{d}_{ij}^{cart}(\boldsymbol{q}_m^{sobol}). \tag{28}$$

Lastly, we use Equation (11) and continue with the trajectory.

While this approach will be less accurate than exactly evaluating $\boldsymbol{d}_{ij}$ at each classical time step, it will also be less costly since we perform only N_{sobol} evaluations of the NACs. In our examples, we have $N_{sobol} = 10000$, and with possibly thousands of members of a trajectory swarm, the computational savings quickly become apparent. Furthermore, the maximum nearest-neighbor distance of the Sobol points is at most 0.02, so we have a robust set of data with which to compute (28).

3 Results and Discussion

In this section, we describe the simulation setup and present *ab initio* results for our test reaction: the photodissociation of gaseous azomethane in a vacuum.

3.1 Electronic structure calculations (offline)

We perform ground-state density-functional theory (DFT) optimizations of azomethane at the nodes of the mixed-basis grid in Gaussian 16[99] at the B3LYP/6-311G* level of theory.[100–104] After each geometry optimization, we perform stability analysis[105] to determine whether a closed- or open-shell wavefunction yields lower energy. If an instability is found, the geometry is reoptimized. We use Orca v4.2.1[106,107] to compute $S_0 \to S_1$ excitation energies (TD-DFT) at the optimized ground-state geometries, as well as Hellmann–Feynman nonadiabatic couplings at the Sobol' points (CIS). We use the stability-tested wavefunction to compute the NACs. We have included example input files for Gaussian and Orca in Sec. 2 of the ESI.† We refine the sparse grid until the energy differences of the minima and transition states on the S_0 surface are within ∼5% or ∼1 kcal/mol of their Gaussian-optimized value (ESI Tables S1 and S2)† and $\boldsymbol{X}(\boldsymbol{q})$ is smoothly varying. The final mixed-basis grid (see ESI) has 7215 nodes.†

We have previously described the design variables $\boldsymbol{q}$ (Fig. 1) in great detail elsewhere,[61] but we briefly reiterate them here. Table 1 summarizes the $d = 5$ design variables we use for this study, chosen to capture rotation, inversion, and dissociation transition states. As noted previously, these design variables come from a previous study of dimension-reduced azomethane photodynamics, namely Cattaneo and Persico's 2001 study.[68] A preliminary 1998 study by Cattaneo and Persico[66] simplified the molecular geometry by treating the two methyl groups as point masses, which unfortunately eliminated several high- and low-frequency normal modes.[68] We opted to include the two methyl dihedrals not only to capture two of the low-frequency modes, like Cattaneo and Persico's 2001 study, but also to ensure smoothness of the interpolated $\boldsymbol{X}(\boldsymbol{q})$.

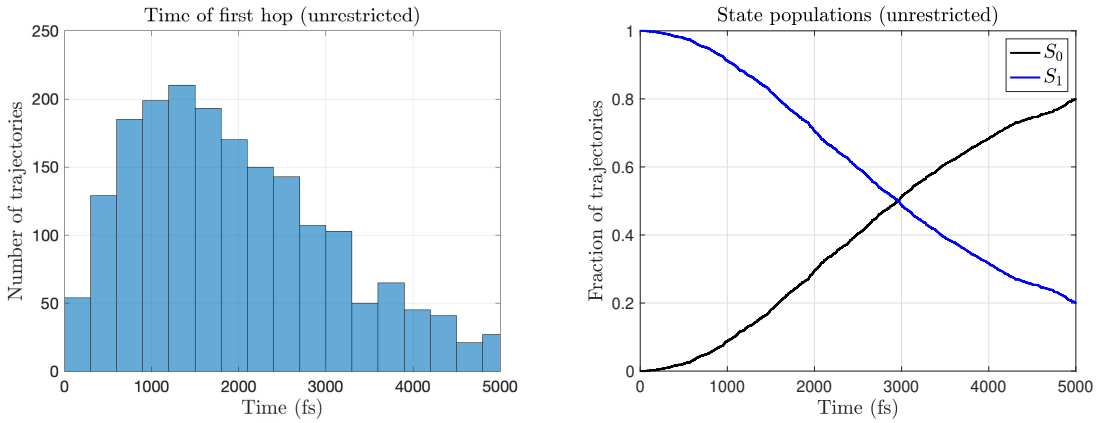

(a) (b)

Fig. 3 (a) First hopping times using unrestricted PESs and NACs. (b) State populations for the same.

Table 1 List of design variables from Fig. 1

Label	Structural coordinate	Domain	Periodic?
q_1	C^2–N^2–N^1–C^1 torsion	$[-180, 180]$ deg	Y
q_2	N^2–N^1–C^1–H torsion	$[-180, 180]$ deg	Y
q_3	N^1–N^2–C^2–H′ torsion	$[-180, 180]$ deg	Y
q_4	N^1–C^1 distance	$[1.1, 2.5]$ Å	N
q_5	N^2–N^1–C^1 angle	$[90, 270]$ deg	N

As described previously,[61] since q_5 can be linear or larger than 180°, we must do internal bookkeeping to encode the variables appropriately in an electronic structure program. Specifically, if $q_5 > 180$, then we add q_1 to 180° and subtract q_5 from 360. Since the linear structure is within the q_5 domain, we also must take care to avoid multivalued geometries as $q_5 \to 180$. We accomplish this by offsetting q_2 by $(q_1 + 180)$ whenever $q_5 \neq 180$. We include several animations in the ESI† to demonstrate the smoothness of $\boldsymbol{X}(\boldsymbol{q})$ and to motivate our definition of q_2.

In Fig. 2(a), we show a slice of the mixed-basis S_0 and S_1 PESs constructed with stability checks. Unlike previous work,[66,69] the unrestricted PES does not have a crossing seam, leading to small nonadiabatic coupling between the S_0 and S_1 surfaces. Indeed, we will demonstrate this phenomenon in the following section with a surface hopping swarm; see Figs. 3, 4(c), and 4(e) and associated discussion. To capture the crossing seam, we construct the S_0 PES by performing single-point energy calculations with restricted (closed-shell) wavefunctions at the geometries that were optimized with stability checks. We do this because directly performing constrained optimizations with restricted wavefunctions yielded undesirable structures, in which hydrogen atoms migrate between the C and N atoms. We show the resulting restricted S_0 PES in Fig. 2(b). For this PES, we compute the couplings using restricted wavefunctions only. We did not observe meaningful changes in the S_1 PES between the two cases. Therefore, in both cases we employed the S_1 PES constructed from the TD-DFT calculations using the restricted S_0 PES as a reference.

3.2 Surface hopping swarm (online)

We sample 2000 initial geometries and momenta by running a reduced-dimensional Langevin thermostat[56,61] on the S_0 PES at 298.15 K ($\gamma = 0.01$ fs^{-1}), starting at the *trans*- conformation. The experimental boiling point of azomethane at 1 atm is 273.45 K,[108] which ensures that we are in the gaseous regime. We integrate the Langevin equations for a burn-in period of 10 ps and then sample every 20 fs to construct an ensemble of $\boldsymbol{q}_0$ and $\boldsymbol{p}_0$, similarly to Cattaneo and Persico.[66,68]

For each ensemble member, we excite vertically to the S_1 surface but keep $\boldsymbol{q}_0$ and $\boldsymbol{p}_0$ unchanged. We integrate the classical dynamics (2) with a time step of $\Delta t_c = 0.25$ fs and the quantum amplitudes (13) with $\Delta t_q = 0.01$ fs, up to 5 ps. The transition probabilities and momenta adjustments (including for frustrated hops) are given in Section 2.2. We approximate the NACs according to Section 2.4 using 10000 space-filling Sobol' points† and the cutoff radius $R = 0.05$. The computing environment is XSEDE Bridges-2,[109,110] where each trajectory receives 2 GB RAM and one core of an AMD EPYC 7742 CPU. All codes are freely available on GitHub.**

We show the results of surface hopping with the unrestricted PES and couplings in Fig. 3. The median hopping time is 1760 fs, which is far larger than previous theoretical predictions of 100–500 fs.[66–71] Indeed, more than 50% of trajectories are in the S_1 state until 3 ps, and more than 20% are still in S_1 after 5 ps [Fig. 3(b)]. Therefore, we now use the restricted S_0 PES described in the previous section. We compare the maximum elements of the NAC vectors between the two cases, and we find that S_0/S_1 couplings are 20 times larger for the restricted S_0 surface than for the unrestricted S_0 surface. We explain this observation by noting that the unrestricted S_0 PES exhibits an avoided crossing near $q_1 \approx \pm 90$, while the restricted S_0 PES shows a crossing seam in the same region.

We show the results for the restricted PES in Fig. 4. An animation of one trajectory is also in the ESI,† which visually demon-

** https://github.com/zbmorrow/rrFSSH

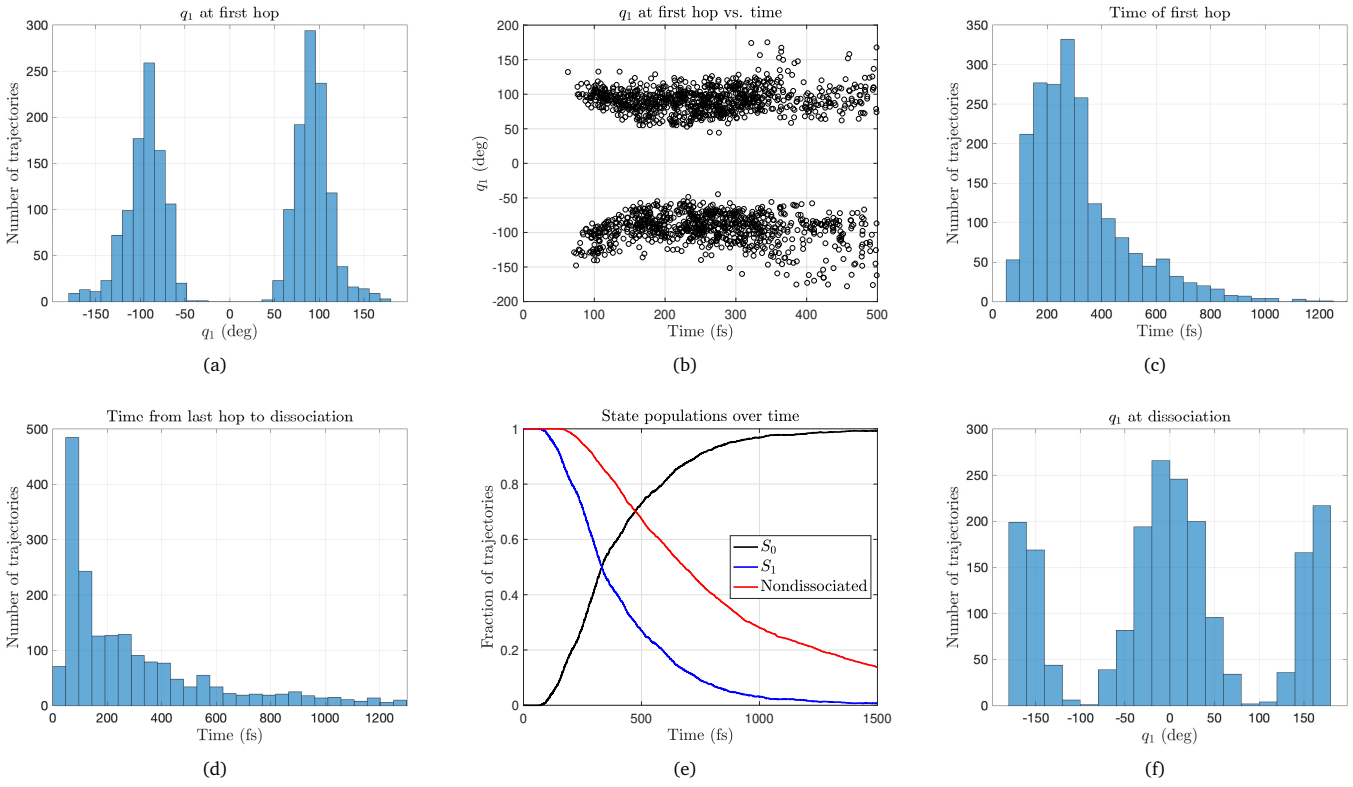

Fig. 4 Results using the restricted PESs and NACs. (a) Values of q_1 at first hop. (b) Values of q_1 vs time of first hop. (c) Time of first $S_1 \to S_0$ transition. (d) Lag between final $S_1 \to S_0$ transition and dissociation. (e) Populations of the S_0/S_1 states and nondissociated molecules. (f) Values of q_1 at dissociation.

strates the relaxation on S_1 and S_0, as well as the ability of $\boldsymbol{X}(\boldsymbol{q})$ to reconstruct the geometry accurately. All trajectories dissociated within 5 ps (defined as $q_4 > 2.5$ Å), and all dissociations occur on the S_0 surface. From Figs. 4(a) and 4(b), we can see that the molecule is near the S_0/S_1 crossing seam ($q_1 \approx \pm 90°$) when the first hop occurs. The slight curvature in the swarms of Fig. 4(b) reflects the geometry of the molecule cycling through the minimum on the S_1 surface. The median time of first hop is 276 fs [Fig. 4(c)], and the median lag time between final hop and dissociation is 224 fs [Fig. 4(d)], implying that dissociation happens relatively quickly after internal conversion (IC). We fit the S_1 and nondissociated populations of Fig. 4(e) to the exponential decay function

$$y = \exp\left(-(t - t_1)/t_2\right) \tag{29}$$

where t_1 and t_2 are the latency and decay times, respectively. The overall lifetime is $\tau = t_1 + t_2$. For the S_1 population, we obtain $t_1 = 78$ fs and $t_2 = 342$ fs, yielding a lifetime of $\tau = 420$ fs. For the lifetime of the nondissociated molecule, we find $t_1 = 188$ fs and $t_2 = 675$ fs, yielding a lifetime of $\tau = 863$ fs. We note that the latency time of the nondissociated population decay is smaller than the lifetime of the S_1 population, again showing an overlap between the time scales of IC and dissociation.

Fig. 4(f) shows the values of q_1 at dissociation. Upon dissociation, we find very few trajectories in the vicinity of the crossing seam; most have relaxed into either *cis-* or *trans-* structures. If we define *trans-* as $q_1 \in [-180, -150] \cup [150, 180)$ and *cis-* as $q_1 \in [-30, 30]$ (for $q_5 < 180$),[66,68] then 31% of trajectories ended in *trans* and 37% in *cis*. This is in agreement with the vibrational frequency of C–N–N–C torsion (290.90 cm^{-1}), which yields a period of 115 fs. Since dissociation occurs around 224 fs after the last hop (in the median), then there is ample time to relax to the *cis-* or *trans-* conformations.

We also test the robustness of our method with respect parameter choices by altering various values while holding all others constant: $\Delta t_c = 0.05$ fs, $\Delta t_q = 0.001$ fs; $N_{sobol} = 5000$; $N_{sobol} = 1000$; $R = 0.20$; $R = 10^{-4}$ (forced nearest-neighbor); and $R = 10^{-4}$, $N_{sobol} = 1000$. We display the results in Table 2. Our results also appear to be consistent across parameter choices, with the exception of excessively large radius R. Refining the time step does not significantly alter the results. Similarly, forcing the nearest-neighbor NAC approximation ($R = 10^{-4}$) does not cause a large change in the outputs. The nearest-neighbor NAC approximation appears to comparable in accuracy to the weighted average—without needing to compute exponential weights. Furthermore, if the evaluation of the NACs in the offline phase is quite costly, these results indicate that one may use a smaller number of Sobol' points ($N_{sobol} = 5000$, $d = 5$) to obtain lifetimes in agreement with previous *ab initio* studies. However, if N_{sobol} is too small, the accuracy tends to degrade somewhat ($N_{sobol} = 1000$ in our examples).

Table 2 Comparison of results for various parameter modifications. Section 2.4 discusses N_{sobol} and R, while Δt_c and Δt_q were described earlier in this section.

	S_1 time constants					
Alteration	t_1 (fs)	t_2 (fs)	τ (fs)	Med. hop–dissoc. gap (fs)	% yield, *trans-*	% yield, *cis-*
None (baseline)	78	342	420	224	31	37
$\Delta t_c = 0.05$, $\Delta t_q = 0.001$	108	285	393	232	33	36
$N_{sobol} = 5000$	119	324	443	232	29	39
$N_{sobol} = 1000$	140	407	547	241	37	33
$R = 0.20$	190	790	980	230	36	34
$R = 10^{-4}$	109	290	399	236	30	37
$N_{sobol} = 1000$, $R = 10^{-4}$	142	404	546	236	37	32

3.3 Discussion

The photochemical and thermal properties of azoalkanes have a long history of study,[69,111–113] particularly azomethane, as the simplest member of this class of compounds. This wealth of prior work makes azomethane a desirable test system. A series of studies within the last three decades has established that the photodissociation of azomethane happens stepwise in the S_0 state:[62,64–66,68]

$$CH_3NNCH_3 \rightarrow CH_3NN\cdot + CH_3\cdot \tag{30}$$

$$CH_3NN\cdot + CH_3\cdot \rightarrow N_2 + 2CH_3\cdot \tag{31}$$

with the second dissociation quickly (femtosecond-level) following the first. Because this reaction mechanism is well-established, we include only one C–N bond length in our design variables, focusing on the first step of the mechanism. We compare the results of our reduced-dimensional method to previous experimental and highly accurate full-dimensional *ab initio* results in terms of excited-state lifetimes and lifetimes of the nondissociated molecule. Since there are various setup parameters across the studies, we opt to discuss in paragraph rather than tabular form.

Recent literature is in very good agreement on the lifetime of azomethane in the S_1 state: 70–100 fs (experimental)[65] and 100–500 fs (theoretical).[66–71] The spread within theoretical results is largely due to a variety of model chemistries and simulation parameters. Using a custom-built diabatic wavefunction, Cattaneo and Persico found the majority of first hops occurring before 400 fs, with an S_1 lifetime of approximately 400 fs.[66–68] With complete active space (CAS) and multireference configuration interaction (MRCI) calculations, Sellner and coworkers computed an S_1 lifetime of 163–191 fs using a Wigner distribution of initial conditions and no additional torsional bias.[69] Around the same time, Ruckenbauer and coworkers computed an S_1 lifetime of 113 fs, using CAS-type methods and Wigner-distributed initial conditions.[70] Studies using the multiple spawning method obtained S_1 lifetimes of 125–150 fs, though dissociation was either absent or rare.[72,73] Recently, Minezawa and Nakajima developed a surface hopping framework using spin-flip TD-DFT and obtained an S_1 lifetime of 155 fs, though simulations were terminated before finding dissociation.[71]

Our computed least-squares lifetime of $\tau = 420$ fs, obtained with reduced-dimensional dynamics and a relatively simple underlying model chemistry, is in excellent agreement with Cattaneo and Persico's $S_1 \rightarrow S_0$ hopping results. The shorter lifetimes found by recent studies can be attributed to performing direct dynamics with a custom or more computationally intensive model chemistry, versus a surrogate PES built with B3LYP/6-311G*. Furthermore, we emphasize that previous studies either treated the methyl groups as point masses[66] or used the full Cartesian geometry within the dynamics,[68–70] whereas we use a relaxed PES involving only the important reaction coordinates.

As noted by Sellner and coworkers,[69] the time scale of dissociation following $S_0 \leftarrow S_1$ de-excitation is the subject of interesting, unresolved debate. Dissociation occurs either on a picosecond time-scale after relaxation to *trans-* or *cis-* conformations (statistical model), or on a femtosecond time-scale shortly after de-excitation (impulsive model). Lee's group observed experimental results favoring the statistical model,[62,63] while the experimental findings of Zewail's group favor the impulsive model.[64,65] As noted by Zewail's group in *Science*, many fast femtosecond-level reactions do in fact occur, though they violate Rice–Ramsperger–Kassel–Marcus (RRKM) theory and the underlying assumption of statistical redistribution of vibrational energy.[114]

In spite of the split experimental findings, all recent *ab initio* simulations of azomethane photodissociation favor the statistical model. Cattaneo and Persico[68] observed only 20% of dissociations within 1 ps of initial $S_0 \rightarrow S_1$ excitation, with 10% occurring before 400 fs and almost none before 250 fs. The same study required 100 ps before 75% of trajectories dissociated. Using the NEWTON-X package,[28] Sellner et al observed a small number of dissociations (∼5%) prior to 500 fs when additional vibrational quanta are added to the torsional rotation; without additional torsional bias, no dissociations occurred prior to 500 fs.[69] Ruckenbauer and coworkers observed a small number (∼5%) of sub-picosecond dissociations, occurring within 350 fs of de-excitation.[70]

Unlike previous *ab initio* studies, our results favor a dissociation time faster than the ∼ 1 ps prediction of the statistical model. Experimentally, Zewail's group found a 70–100 fs rise time of the $CH_3NN\cdot$ fragment, clearly favoring the impulsive model. In our simulations, 50% of trajectories dissociated within 700 fs of initial $S_0 \rightarrow S_1$ excitation and 72% within 1 ps, so subpicosecond dissociation is dominant. Moreover, our median time between the last hop and dissociation is on the order of 200 fs; there are intermediate hops back to S_1 before the trajectory finally settles

on S_0. Though our results do not resolve the statistical–impulsive debate, they provide evidence that the impulsive findings of Zewail's group merit further study and could be justifiable on *ab initio* grounds.

4 Conclusions and Future Work

This paper has presented a framework for trajectory surface hopping simulations in a reduced-dimensional setting, using only the important reaction coordinates of the system, as determined by the user. We have also presented a method for computing a modest number of nonadiabatic coupling vectors in the offline phase and then querying them in the online phase. This method is implemented in Python and freely available on GitHub.[||] When applied to azomethane photodissociation, this method produces excited-state lifetimes that are consistent with previous theoretical and experimental studies. We have demonstrated that our method is robust with respect to the choice of parameters used to perform time integration and approximate the nonadiabatic couplings. Lastly, our method unveils fast, femtosecond-level dissociation after $S_0 \leftarrow S_1$ de-excitation that has previously only been demonstrated experimentally, not computationally, in the literature.

Possible future directions and extensions include the use of automated design-variable selection,[33] incorporating various statistical modifications to account for phenomena in different physical regimes,[1,2,79] and applications to larger molecules. Of particular interest are the surface-crossing dynamics of Fe(II) polypyridine complexes,[9] which have applications in photovoltaics.

Conflicts of interest

There are no conflicts to declare.

Acknowledgements

Z.M. is thankful for a National Science Foundation (NSF) Graduate Research Fellowship (DGE-1746939). H.Y.K. and E.J. received support from the NSF (CHE-1554855). C.T.K. was funded by the NSF (DMS-1745654, DMS-1906446).

This work used the Extreme Science and Engineering Discovery Environment (XSEDE), which is supported by the NSF (ACI-1548562).[109] Specifically, it used the Bridges-2 system, which is supported by the NSF (ACI-1928147), at the Pittsburgh Supercomputing Center (PSC).[110] We acknowledge the computing resources provided on Henry2, a high-performance computing cluster operated by North Carolina State University.

Notes and references

1 L. Wang, A. Akimov and O. V. Prezhdo, *J. Phys. Chem. Lett.*, 2016, **7**, 2100–2112.

2 F. Plasser, M. Barbatti, A. J. A. Aquino and H. Lischka, *Theor. Chem. Acc.*, 2012, **131**, 1–14.

3 D. Polli, P. Altoè, O. Weingart, K. M. Spillane, C. Manzoni, D. Brida, G. Tomasello, G. Orlandi, P. Kukura, R. A. Mathies, M. Garavelli and G. Cerullo, *Nature*, 2010, **467**, 440–443.

4 R. González-Luque, G. Olaso-González, M. Merchán, P. B. Coto, L. Serrano-Andrés and M. Garavelli, *Int. J. Quantum Chem.*, 2011, **111**, 3431–3437.

5 G. Olaso-González, D. Roca-Sanjuán, L. Serrano-Andrés and M. Merchán, *J. Chem. Phys.*, 2006, **125**, 231102.

6 C. Daniel, J. Full, L. Gonzalez, C. Lupulescu, J. Manz, A. Merli, S. Vajda and L. Wöste, *Science*, 2003, **299**, 536–539.

7 W. R. Duncan, W. M. Stier and O. V. Prezhdo, *J. Am. Chem. Soc.*, 2005, **127**, 7941–7951.

8 C. F. Craig, W. R. Duncan and O. V. Prezhdo, *Phys. Rev. Lett.*, 2005, **95**, 163001.

9 J. Nance, D. N. Bowman, S. Mukherjee, C. T. Kelley and E. Jakubikova, *Inorg. Chem.*, 2015, **54**, 11259–11268.

10 R. Long, O. V. Prezhdo and W. Fang, *WIREs Comput. Mol. Sci.*, 2017, **7**, e1305.

11 D. Fazzi, M. Barbatti and W. Thiel, *Phys. Chem. Chem. Phys.*, 2015, **17**, 7787–7799.

12 Y. Shang, Q. Li, L. Meng, D. Wang and Z. Shuai, *Theor. Chem. Acc.*, 2011, **129**, 291–301.

13 J.-L. Brédas, J. E. Norton, J. Cornil and V. Coropceanu, *Acc. Chem. Res.*, 2009, **42**, 1691–1699.

14 T. Petrenko and F. Neese, *J. Chem. Phys.*, 2007, **127**, 164319.

15 M. Barbatti, A. J. A. Aquino and H. Lischka, *Phys. Chem. Chem. Phys.*, 2010, **12**, 4959–4967.

16 M. Stenrup and A. Larson, *Chem. Phys.*, 2011, **379**, 6–12.

17 R. Kapral, *Annu. Rev. of Phys. Chem.*, 2006, **57**, 129–157.

18 P. Ehrenfest, *Z. Phys.*, 1927, **45**, 455–457.

19 O. V. Prezhdo and V. V. Kisil, *Phys. Rev. A*, 1997, **56**, 162–175.

20 T. J. Martinez, M. Ben-Nun and R. D. Levine, *J. Phys. Chem.*, 1996, **100**, 7884–7895.

21 M. Ben-Nun and T. J. Martínez, *J. Chem. Phys.*, 1998, **108**, 7244–7257.

22 T. J. Martínez, *Acc. Chem. Res.*, 2006, **39**, 119–126.

23 A. M. Virshup, C. Punwong, T. V. Pogorelov, B. A. Lindquist, C. Ko and T. J. Martínez, *J. Phys. Chem. B*, 2009, **113**, 3280–3291.

24 R. K. Preston and J. C. Tully, *J. Chem. Phys.*, 1971, **54**, 4297–4304.

25 J. C. Tully, *J. Chem. Phys.*, 1990, **93**, 1061–1071.

26 S. Hammes-Schiffer and J. C. Tully, *J. Chem. Phys.*, 1994, **101**, 4657–4667.

27 O. V. Prezhdo and P. J. Rossky, *J. Chem. Phys.*, 1997, **107**, 825–834.

28 M. Barbatti, M. Ruckenbauer, F. Plasser, J. Pittner, G. Granucci, M. Persico and H. Lischka, *WIREs Comput. Mol. Sci.*, 2014, **4**, 26–33.

29 R. Send and F. Furche, *J. Chem. Phys.*, 2010, **132**, 044107.

30 I. F. Galván, M. G. Delcey, T. B. Pedersen, F. Aquilante and R. Lindh, *J. Chem. Theory Comput.*, 2016, **12**, 3636–3653.

31 D. B. Lingerfelt, D. B. Williams-Young, A. Petrone and X. Li, *J. Chem. Theory Comput.*, 2016, **12**, 935–945.

32 W. Li and A. Ma, *J. Chem. Phys.*, 2016, **144**, 114103.

33 S. R. Hare, L. A. Bratholm, D. R. Glowacki and B. K. Carpenter, *Chem. Sci.*, 2019, **10**, 9954–9968.

34 A. Albaugh, H. A. Boateng, R. T. Bradshaw, O. N. Demerdash, J. Dziedzic, Y. Mao, D. T. Margul, J. Swails, Q. Zeng, D. A. Case, P. Eastman, L.-P. Wang, J. W. Essex, M. Head-Gordon, V. S. Pande, J. W. Ponder, Y. Shao, C.-K. Skylaris, I. T. Todorov, M. E. Tuckerman and T. Head-Gordon, *J. Phys. Chem. B*, 2016, **120**, 9811–9832.

35 J. M. Bowman, G. Czakó and B. Fu, *Phys. Chem. Chem. Phys.*, 2011, **13**, 8094–8111.

36 A. Brown, B. J. Braams, K. Christoffel, Z. Jin and J. M. Bowman, *J. Chem. Phys.*, 2003, **119**, 8790–8793.

37 B. J. Braams and J. M. Bowman, *Int. Rev. Phys. Chem.*, 2009, **28**, 577–606.

38 B. Jiang, J. Li and H. Guo, *Int. Rev. Phys. Chem.*, 2016, **35**, 479–506.

39 S. Manzhos, R. Dawes and T. Carrington, *Int. J. Quantum Chem.*, 2014, **115**, 1012–1020.

40 Q. Lin, L. Zhang, Y. Zhang and B. Jiang, *J. Chem. Theory Comput.*, 2021, **17**, 2691–2701.

41 G. G. Maisuradze, D. L. Thompson, A. F. Wagner and M. Minkoff, *J. Chem. Phys.*, 2003, **119**, 10002–10014.

42 G. G. Maisuradze and D. L. Thompson, *J. Phys. Chem. A*, 2003, **107**, 7118–7124.

43 R. Farwig, *J. Comput. Appl. Math.*, 1986, **16**, 79–93.

44 Y. Guo, I. Tokmakov, D. L. Thompson, A. F. Wagner and M. Minkoff, *J. Chem. Phys.*, 2007, **127**, 214106.

45 K. C. Thompson, M. J. T. Jordan and M. A. Collins, *J. Chem. Phys.*, 1998, **108**, 8302–8316.

46 M. A. Collins and D. F. Parsons, *J. Chem. Phys.*, 1993, **99**, 6756–6772.

47 M. A. Collins, *Theor. Chem. Acc.*, 2002, **108**, 313–324.

48 M. A. Collins, *Lec. Notes Comput. Sci.*, 2003, 159–167.

49 J. Cui and R. V. Krems, *Phys. Rev. Lett.*, 2015, **115**, 073202.

50 E. Uteva, R. S. Graham, R. D. Wilkinson and R. J. Wheatley, *J. Chem. Phys.*, 2017, **147**, 161706.

51 C. D. Berweger, W. F. van Gunsteren and F. Müller–Plathe, *J. Comput. Chem.*, 1998, **18**, 1484–1495.

52 S. A. Smolyak, *Dokl. Akad. Nauk.*, 1963, **148**, 1042–1045.

53 M. K. Stoyanov and C. G. Webster, *Comput. Math. Appl.*, 2016, **71**, 2449–2465.

54 E. Novak and K. Ritter, *Constr. Approx.*, 1999, **15**, 499–522.

55 K. Hallatschek, *Numer. Math.*, 1992, **63**, 83–97.

56 C. Liu, C. T. Kelley and E. Jakubikova, *J. Phys. Chem. A*, 2019, 4543–4554.

57 J. Nance, E. Jakubikova and C. T. Kelley, *J. Chem. Theory Comput.*, 2014, **10**, 2942–2949.

58 J. Nance and C. T. Kelley, *SIAM J. Sci. Comput.*, 2015, **37**, S137–S156.

59 Z. Morrow and M. Stoyanov, *SIAM J. Sci. Comput.*, 2020, **42**, A2436–A2460.

60 Z. Morrow, C. Liu, C. T. Kelley and E. Jakubikova, *J. Phys. Chem. B*, 2019, **123**, 9677–9684.

61 Z. Morrow, H.-Y. Kwon, C. T. Kelley and E. Jakubikova, *J. Chem. Theory Comput.*, 2021, to appear.

62 S. W. North, C. A. Longfellow and Y. T. Lee, *J. Chem. Phys.*, 1993, **99**, 4423–4429.

63 A. S. Bracker, S. W. North, A. G. Suits and Y. T. Lee, *J. Chem. Phys.*, 1998, **109**, 7238–7245.

64 E. W.-G. Diau, O. K. Abou-Zied, A. A. Scala and A. H. Zewail, *J. Am. Chem. Soc.*, 1998, **120**, 3245–3246.

65 E. W.-G. Diau and A. H. Zewail, *ChemPhysChem*, 2003, **4**, 445–456.

66 P. Cattaneo and M. Persico, *Chem. Phys. Lett.*, 1998, **289**, 160–166.

67 P. Cattaneo and M. Persico, *Theor. Chem. Acc.*, 2000, **103**, 390–398.

68 P. Cattaneo and M. Persico, *J. Am. Chem. Soc.*, 2001, **123**, 7638–7645.

69 B. Sellner, M. Ruckenbauer, I. Stambolić, M. Barbatti, A. J. A. Aquino and H. Lischka, *J. Phys. Chem. A*, 2010, **114**, 8778–8785.

70 M. Ruckenbauer, M. Barbatti, B. Sellner, T. Muller and H. Lischka, *J. Phys. Chem. A*, 2010, **114**, 12585–12590.

71 N. Minezawa and T. Nakajima, *J. Chem. Phys.*, 2019, **150**, 204120.

72 J. Ghosh, S. Bhaumik and A. Bhattacharya, *Chem. Phys.*, 2018, **513**, 221–229.

73 A. Gaenko, A. DeFusco, S. A. Varganov, T. J. Martínez and M. S. Gordon, *J. Phys. Chem. A*, 2014, **118**, 10902–10908.

74 A. Deriglazov, *Classical Mechanics*, Springer-Verlag, Berlin, 2016.

75 C. Lanczos, *The Variational Principles of Mechanics*, Courier Corporation, 2012.

76 C. Störmer, *Arch. Sci. Phys. Nat.*, 1912, **33**, 51–69.

77 L. Verlet, *Phys. Rev.*, 1967, **159**, 98–103.

78 L. Wang, G. Nan, X. Yang, Q. Peng, Q. Li and Z. Shuai, *Chem. Soc. Rev.*, 2010, **39**, 423–434.

79 G. Granucci and M. Persico, *J. Chem. Phys.*, 2007, **126**, 134114.

80 L. Wang, A. E. Sifain and O. V. Prezhdo, *J. Phys. Chem. Lett.*, 2015, **6**, 3827–3833.

81 J. Crank and P. Nicolson, *Math. Proc. Camb. Philos. Soc.*, 1947, **43**, 50–67.

82 W. Gautschi, *Numerical Analysis*, Birkhäuser Basel, 2nd edn, 2012.

83 C. W. Clenshaw and A. R. Curtis, *Numer. Math.*, 1960, **2**, 197–205.

84 M. Stoyanov, *User Manual: TASMANIAN Sparse Grids*, Oak Ridge National Laboratory Technical Report ORNL/TM-2015/596, 2015.

85 M. Stoyanov, *Sparse Grids and Applications–Miami 2016*, Springer, 2018, pp. 175–199.

86 M. Stoyanov, D. Lebrun-Grandie, J. Burkardt and D. Munster, *Tasmanian*, 2013, `https://github.com/ORNL/Tasmanian`.

87 L. D. Landau, *Z. Phys. Sowjetunion*, 1932, **1**, 88–98.

88 C. Zener, *Proc. R. Soc. Lond.*, 1932, **137**, 696–702.

89 C. Wittig, *J. Phys. Chem. B*, 2005, **109**, 8428–8430.

90 J. Suchan, J. Janoš and P. Slavíček, *J. Chem. Theory Comput.*,

2020, **16**, 5809–5820.

91 A. K. Belyaev, C. Lasser and G. Trigila, *J. Chem. Phys.*, 2014, **140**, 224108.

92 H. Niederreiter, *Random Number Generation and Quasi-Monte Carlo Methods*, SIAM, 1992.

93 J. Dick, F. Y. Kuo and I. H. Sloan, *Acta Numer.*, 2013, **22**, 133–288.

94 I. M. Sobol', *USSR Comput. Math. Math. Phys.*, 1967, **7**, 86–112.

95 R. Mukherjee and U. M. Diwekar, *Comput. Chem. Eng.*, 2016, **84**, 28–35.

96 V. Alexandrov, D. Davila, O. Esquivel-Flores, A. Karaivanova, T. Gurov and E. Atanassov, Large-Scale Scientific Computing, 2018, pp. 249–257.

97 R. N. Gantner, L. Herrmann and C. Schwab, *SIAM J. Numer. Anal.*, 2018, **56**, 111–135.

98 Z. He, *SIAM J. Numer. Anal.*, 2019, **57**, 854–874.

99 M. J. Frisch, G. W. Trucks, H. B. Schlegel, G. E. Scuseria, M. A. Robb, J. R. Cheeseman, G. Scalmani, V. Barone, G. A. Petersson, H. Nakatsuji, X. Li, M. Caricato, A. V. Marenich, J. Bloino, B. G. Janesko, R. Gomperts, B. Mennucci, H. P. Hratchian, J. V. Ortiz, A. F. Izmaylov, J. L. Sonnenberg, D. Williams-Young, F. Ding, F. Lipparini, F. Egidi, J. Goings, B. Peng, A. Petrone, T. Henderson, D. Ranasinghe, V. G. Zakrzewski, J. Gao, N. Rega, G. Zheng, W. Liang, M. Hada, M. Ehara, K. Toyota, R. Fukuda, J. Hasegawa, M. Ishida, T. Nakajima, Y. Honda, O. Kitao, H. Nakai, T. Vreven, K. Throssell, J. A. Montgomery, Jr., J. E. Peralta, F. Ogliaro, M. J. Bearpark, J. J. Heyd, E. N. Brothers, K. N. Kudin, V. N. Staroverov, T. A. Keith, R. Kobayashi, J. Normand, K. Raghavachari, A. P. Rendell, J. C. Burant, S. S. Iyengar, J. Tomasi, M. Cossi, J. M. Millam, M. Klene, C. Adamo, R. Cammi, J. W. Ochterski, R. L. Martin, K. Morokuma, O. Farkas, J. B. Foresman and D. J. Fox, *Gaussian 16 Revision A.03*, 2016, Gaussian Inc., Wallingford, CT.

100 A. D. Becke, *J. Chem. Phys.*, 1993, **98**, 5648–5652.

101 A. D. Becke, *J. Chem. Phys.*, 1993, **98**, 1372–1377.

102 C. Lee, W. Yang and R. G. Parr, *Phys. Rev. B*, 1988, **37**, 785–789.

103 P. J. Stephens, F. J. Devlin, C. F. Chabalowski and M. J. Frisch, *J. Phys. Chem.*, 1994, **98**, 11623–11627.

104 R. Krishnan, J. S. Binkley, R. Seeger and J. A. Pople, *J. Chem. Phys.*, 1980, **72**, 650–654.

105 R. Bauernschmitt and R. Ahlrichs, *J. Chem. Phys.*, 1996, **104**, 9047–9052.

106 F. Neese, *WIREs Comput. Mol. Sci.*, 2012, **2**, 73–78.

107 F. Neese, *WIREs Comput. Mol. Sci.*, 2018, **8**, e1327.

108 J. Dykyj, J. Svoboda, R. C. Wilhoit, M. Frenkel and K. R. Hall, *Vapor Pressure and Antoine Constants for Nitrogen Containing Organic Compounds*, Springer-Verlag, 2001, vol. 20C, ch. 2, p. 28.

109 J. Towns, T. Cockerill, M. Dahan, I. Foster, K. Gaither, A. Grimshaw, V. Hazlewood, S. Lathrop, D. Lifka, G. D. Peterson, R. Roskies, J. Scott and N. Wilkins-Diehr, *Comput. Sci. Eng.*, 2014, **16**, 62–74.

110 N. A. Nystrom, M. J. Levine, R. Z. Roskies and J. R. Scott, Proceedings of the 2015 XSEDE Conference: Scientific Advancements Enabled by Enhanced Cyberinfrastructure, New York, 2015.

111 H. C. Ramsperger, *Proc. Nat. Acad. Sci. U.S.A.*, 1927, **13**, 849–853.

112 H. C. Ramsperger, *J. Am. Chem. Soc.*, 1927, **49**, 912–916.

113 P. S. Engel, *Chem. Rev.*, 1980, **80**, 99–150.

114 E. W.-G. Diau, J. L. Herek, Z. H. Kim and A. H. Zewail, *Science*, 1998, **279**, 847–851.